Angular distribution of diffusely transmitted light

M. U. Vera and D. J. Durian
Department of Physics and Astronomy, University of California, Los Angeles, California 90095-1547
(Received 28 July 1995)

The angular dependence of light diffusely transmitted through an opaque medium is shown to depend directly on the reflective nature of the sample boundary, independent of scattering anisotropy. Experimental data are presented for glass frits and for liquid samples, such as colloidal suspensions and aqueous foams, contained in glass cells and placed in either air, water, or glycerin baths. Results compare well with a simple theoretical prediction based on the diffusion approximation and also with random walk simulations. The importance of this work is not only in providing a simple quantitative explanation of a complex transport problem, but in establishing the proper treatment of boundary conditions for diffusion theory analyses of multiple light scattering experiments.

PACS number(s): 05.60.+w, 42.68.Ay, 07.60.−j

I. INTRODUCTION

Multiple scattering processes are important for transport in such diverse systems as neutrons in reactors, electrons in metals and semiconductors, phonons in crystals, molecules in a gas, and photons in opaque forms of condensed matter and in atmospheric or astrophysical structures. Quantities of interest include the fraction of incident particles absorbed, backscattered, or transmitted through a medium and the angular distribution with which they emerge. Often the wavelength of these particles is much smaller than the scattering length, so successive scattering events are independent and interference effects can be ignored. Theoretical study then reduces to solving integro-differential equations for the particle concentration field as a function of position and velocity direction [1]; this has become a well-developed branch of mathematical physics [2,3]. Since numerical solution is often required in such an approach, it is convenient to study transport analytically by making a diffusion approximation [4]. Important issues are then the proper treatment of the source term and boundary conditions and the accuracy of the resulting predictions.

The multiple scattering phenomenon we focus on here is the angular distribution of photons transmitted through an opaque slab and its connection to the probability for photons to either reflect or refract upon striking the sample boundary. Based on the diffusion approximation, our prediction for the probability for a photon to be transmitted between angles $\cos^{-1}(\mu_e)$ and $\cos^{-1}(\mu_e+d\mu_e)$ from the exterior normal is

$$P(\mu_e)/\mu_e = \tfrac{3}{2}(n_e/n_i)^2(z_e+\mu_i)[1-R(\mu_i)] , \qquad (1.1)$$

where n_i and n_e are the refractive indices of the sample interior and exterior, respectively; z_e is a number of order 1, called the extrapolation length ratio, which sets the boundary conditions for the diffuse photon concentration field; $R(\mu_i)$ is the total reflectivity for a photon striking the boundary at $\cos^{-1}(\mu_i)$ from the interior normal; and μ_i and μ_e are related by Snell's law. This generalizes our previous prediction [5] to incorporate two crucial effects that, in general, must not be neglected: refraction and angular dependence of the single-photon boundary reflectivity. While Eq. (1.1) thus represents an important theoretical improvement, it is based on several uncontrolled approximations and must therefore be tested. Here we present a detailed comparison of Eq. (1.1) and its further generalization to polarization dependence, with both random-walk computer simulations and experiments on glass frits, colloidal suspensions, and foams. All three materials are homogeneous in the sense that photon transport in the bulk can be described with a single, well-defined, transport mean free path, but they each have different boundary structures. For the colloidal suspensions, the interior and exterior refractive indices are known. By varying the latter, we find direct evidence that refraction effects are present, in surprisingly good agreement with Eq. (1.1). By varying the particle size, we demonstrate that scattering anisotropy does not significantly influence the form of $P(\mu_e)$, contrary to recent arguments and simulations [6,7]. Also, excellent agreement is found between prediction and experiment for the polarization dependence of $P(\mu_e)$, showing that there is no significant polarization in the photon concentration field and that the polarization of the transmitted light is entirely due to the polarization dependence of the single-photon boundary reflectivity. For the frit and foam samples, by contrast, the boundary structures are not known in advance, but can instead be deduced and understood from measurements of $P(\mu_e)$. We find evidence that photons propagating through a foam travel both through the gas bubbles as well as within the liquid film in between bubbles.

While understanding the functional form and the physical origin of the angular distribution $P(\mu_e)$ is of general interest in its own right, our motivation is also to address the boundary conditions, as specified by z_e, which should be used in diffusion theory treatments of transport. In this regard, the measurements presented here provide experimental support for our earlier prediction [5,8] that

the value of z_e is intimately connected with the angular distribution of the transmitted light and can thus be studied experimentally. This issue is crucial for an accurate analysis of data obtained with the multiple light scattering techniques known as diffuse-transmission spectroscopy (DTS) [9] and diffusing-wave spectroscopy (DWS) [10]. These diffusing-light spectroscopies have recently been established as useful probes of the structure and dynamics of naturally opaque materials such as dense colloidal suspensions, foams, and emulsions. In DTS, the average fraction T of incident light transmitted through a slab is measured and analyzed in terms of the photon transport mean free path l^* as a probe of the structure of the medium. In DWS, fluctuations in the transmitted light are measured, expressed in terms of the normalized electric field autocorrelation function $g_1(\tau)$, and analyzed in terms of the mean-squared displacement of the scattering sites $x = k^2\langle \Delta r^2(\tau)\rangle$, where k is the wave vector of light in the medium. Assuming that incident photons are all deposited at one transport mean free path in from the edge of a slab of thickness L [11], the diffusion theory predictions used for data analysis are

$$T = \frac{1+z_e}{(L/l^*)+2z_e} , \tag{1.2}$$

$$g_1(x) = \frac{(L/l^*)+2z_e}{1+z_e} \frac{\sinh\sqrt{x} + z_e\sqrt{x}\cosh\sqrt{x}}{(1+z_e^2 x)\sinh\sqrt{(L/l^*)^2 x} + 2z_e\sqrt{x}\cosh\sqrt{(L/l^*)^2 x}} \tag{1.3}$$

and thus depend on the value assumed for z_e. The accuracy of these expressions has been tested by random-walk computer simulations in Refs. [5,12] for boundaries with angle-independent reflectivity and is found to be on the order of 1% or 2% for $L > 5l^*$ and sufficiently small values of x. At issue, then, is how to choose z_e for a given experimental situation so that the desired unknowns l^* and x can be accurately deduced from Eqs. (1.2)–(1.3). Based on measurements of $P(\mu_c)$, we recommend specific values of z_e for analysis of DTS and DWS data on glass fits, colloidal suspensions, and foams. Our procedures can be followed to obtain accurate values of z_e for other, unknown, samples.

The manuscript is organized as follows. In Sec. II we review the basis of the diffusion theory predictions and extend earlier work [5] to properly include the effects of both refraction and an angle- and polarization-dependent boundary reflectivity. In Secs. III and IV, we test these predictions for three distinct scattering media, having different boundary effects, by comparison with experiment and random-walk simulations. In Sec. IV, we summarize the results and conclude with a discussion of how to deduce z_e for an unknown sample from Eq. (1.1) and measurements of the angular distribution of the transmitted light.

II. DIFFUSION THEORY

The simplest description of transport in an opaque material involves a diffusion approximation in which the velocity distribution of the photons (or other such particles) in every volume element is assumed to be isotropic. All observable quantities are then deduced from the diffuse photon concentration field $U(\vec{r})$, which satisfies the diffusion equation with coefficient $D = \frac{1}{3}cl^*$, where c is the speed of light in the material and l^* is the photon transport mean free path [4]. To account more accurately for behavior near the boundaries, where the velocity distribution is not isotropic, one must employ a more sophisticated approach as in the theory of radiative transfer [1,13,14]. The boundary conditions that uniquely specify $U(\vec{r})$ for a given sample geometry and source term are chosen to compensate for this shortcoming of the diffusion approximation [15,16]. The most general boundary condition is for $U(\vec{r})$ to extrapolate to zero at a distance $z_e l^*$ outside the sample; z_e is thus a phenomenological parameter of order 1 appearing in all diffusion theory predictions, as in Eqs. (1.2) and (1.3), and is called the extrapolation length ratio. The value of z_e is prescribed so that the flux J_{in}^R, of photons reflecting from the boundary back into the sample equals the fictitious flux J_{in}^O of photons entering the sample from outside. These fluxes are computed from a kinetic argument by integrating over the sample interior and exterior, respectively,

$$J_{\text{in}}^R \propto \int_0^1 d\mu \int_0^\infty r^2 dr [z_e + \mu r] \frac{\mu}{r^2} e^{-r} R(\mu) = \tfrac{1}{2} R_1 z_e + \tfrac{1}{3} R_2 , \tag{2.1}$$

$$J_{\text{in}}^O \propto \int_0^1 d\mu \int_0^\infty r^2 dr [z_e - \mu r] \frac{\mu}{r^2} e^{-r} = \tfrac{1}{2} z_e - \tfrac{1}{3} . \tag{2.2}$$

The term in square brackets represents the photon concentration in a toroidal volume element $2\pi r^2 d\mu\, dr$ at distance rl^* from the origin and angle $\cos^{-1}\mu$ from the boundary normal; note that the linear increase in concentration with depth $\mu r l^*$ is a solution of the diffusion equation only if there is no absorption, as assumed here. The μ/r^2 term is proportional to the fraction of those photons headed toward a unit area at the origin. With the assumption of isotropic scattering, the exponential term is proportional to the fraction of those that do not scatter before reaching the boundary. Finally, $R(\mu)$ is the total reflection probability for photons striking the sample boundary at angle $\cos^{-1}\mu$ from the normal; the reflectivity moments in Eq. (2.1) are defined as

$$R_n \equiv \int_0^1 (n+1)\mu^n R(\mu) d\mu . \tag{2.3}$$

Note that no assumptions have been made in Eqs.

(1.2)–(1.3) about whether reflections are specular or refraction occurs. For consistency, $J_{\text{in}}^{R}=J_{\text{in}}^{O}$, the value of the extrapolation length ratio must be taken as

$$z_e=\frac{2}{3}\frac{1+R_2}{1-R_1} . \tag{2.4}$$

This derivation of the boundary conditions makes crucial use of the diffusion approximation near the boundaries, where it is least accurate. Further assumptions are that there is no polarization dependence in the photon concentration field and that the photon scattering mean free path l_s is equal to the transport mean free path l^*. These are all uncontrolled approximations that cannot be avoided within a diffusion theory. The latter assumption is especially unwarranted, since in general the scattering is anisotropic with $l^*=l_s/\langle 1-\cos\theta\rangle$, θ being the scattering angle [4]. For many cases of experimental interest, the scattering is primarily into the forward direction, giving $l^* \gg l_s$. Nevertheless, as we shall demonstrate in Sec. IV, predictions based on the diffusion approximation are remarkably accurate if the boundary conditions are treated properly according to Eqs. (2.3) and (2.4).

Given the diffuse photon concentration field specified by z_e, the angular distribution of the exiting photons can be calculated by a kinetic argument similar to Eqs. (2.1) and (2.2) but without integrating over μ [5]. The probability $P_D(\mu_e)d\mu_e$ for a transmitted photon of polarization state D to exit between $\cos^{-1}\mu_e$ and $\cos^{-1}(\mu_e+d\mu_e)$ from the exterior normal is given by integrating over space within the corresponding conic shell inside the sample:

$$P_D(\mu_e)d\mu_e \propto d\mu_i \int_0^\infty r^2 dr[z_e+\mu_i r]\frac{\mu_i}{r^2}e^{-r}[1-R^D(\mu_i)] . \tag{2.5}$$

$R^D(\mu_i)$ is the reflection probability for photons of polarization state D striking the sample boundary at an angle $\cos^{-1}\mu_i$ from the interior normal. Carrying out the integration and using a consequence of Snell's law, $d\mu_e/d\mu_i=n_i^2\mu_i/n_e^2\mu_e$, where n_i and n_e are, respectively, the interior and exterior refractive indices, yields the following prediction for the angular distribution of diffusely transmitted light:

$$P_D(\mu_e)/\mu_e \propto (z_e+\mu_i)[1-R^D(\mu_i)] , \tag{2.6}$$

where the proportionality constant is set by normalization $\int_0^1 P_D(\mu_e)d\mu_e=1$. For the total distribution, with unpolarized detection, the normalization can be computed directly in terms of the moments of $R(\mu)$, giving the result quoted earlier in the Introduction:

$$P(\mu_e)/\mu_e=\tfrac{3}{2}(n_e/n_i)^2(z_e+\mu_i)[1-R(\mu_i)] . \tag{2.7}$$

This prediction applies for any stratified dielectric boundary profile with the specified interior and exterior refractive indices. For the case of polarized detection, the normalization of Eq. (2.6) cannot similarly be written in a simple closed form. For the case considered in our earlier work [5] that the reflectivity is independent of polarization and angle and that there is no refraction, Eq. (2.7) reduces to

$$P(\mu)/\mu=(z_e+\mu)/(\tfrac{1}{2}z_e+\tfrac{1}{3}) . \tag{2.8}$$

These forms are convenient for comparison with experiment, since the left-hand side can be measured and the right-hand side can be computed. In general, the angular distribution of diffusely transmitted light is expected to be primarily a mixture of cosine and cosine-squared terms whose relative strengths depend on the average boundary reflectivity through the value of z_e. The quantitative shape, however, depends on details of the angle-dependent reflectivity and refraction effects.

In Refs. [5,8], Eq. (2.8) was shown to agree quite well with random-walk computer simulations for several angle-independent boundary reflectivities, independent of the degree of scattering anisotropy. However, many experimental systems of interest, such as colloidal suspensions or foams, are liquid and so must be held in glass sample cells for study by diffusing light spectroscopies. In such cases, boundary reflections occur with angle- and polarization-dependent probability according to Fresnel's law from both the *inner* and *outer* surfaces of the glass boundary. The total boundary reflectivity $R(\mu_i)$ for a photon striking the interior boundary at an angle $\cos^{-1}\mu_i$ should then be obtained by incoherently summing over all multiple reflections. This gives

$$R(\mu_i)=\frac{R_{ab}+R_{bc}-2R_{ab}R_{bc}}{1-R_{ab}R_{bc}} , \tag{2.9}$$

where R_{xy} is the Fresnel reflectivity for interface xy at the appropriate angle given by Snell's law. Both polarization states should be included in the R_{xy}'s for computing z_e from Eqs. (2.3)–(2.4), while only the polarization state D being detected should be included for computation of the $1-R^D(\mu_i)$ term in the angular distribution of Eq. (2.6). Reflectivity moments and extrapolation length ratios calculated according to Eqs. (2.3), (2.4), and (2.9) and Fresnel's laws [17] are collected in Table I for several combinations of interior, wall, and exterior refractive indices to be tested in Sec. IV. Extrapolation length ratio predictions are plotted in Fig. 1 vs interior index for other combinations of wall and exterior indices that may be of experimental relevance using DTS or DWS. Note that these values do not apply if an integrating sphere is mounted to the sample for collection of diffusely transmitted or backscattered light, since reflections from the sphere back into the sample must then be included as an additional contribution to the total boundary reflectivity.

III. EXPERIMENTAL METHOD

The form of the angular distribution of diffusely transmitted light $P(\mu)$ can be measured by moving a small detector in a semicircle about the sample. This is the proper experiment for comparison with the diffusion theory predictions of Sec. II since the probability for transmission within a conic shell is $P(\mu)\Delta\mu \propto P(\mu)\sin\theta$ and the probability for the transmitted photon to be at

TABLE I. Reflectivity moments and extrapolation length ratios computed for opaque media with the specified refractive index profiles at the boundary. The value of $\cos^{-1}(\mu_e^{\min})$ is the farthest angle away from the normal at which transmitted light can emerge, according to Snell's law.

Interior	Wall	Exterior	$\mu_e^{\min}$	R_0	R_1	R_2	z_e
1.33	1.52	1	0	0.6960	0.490 4	0.351 0	1.768
1.33	1.52	1.33	0	0.1745	0.056 29	0.027 36	0.7258
1.33	1.52	1.47	0.426	0.1259	0.034 39	0.015 43	0.7011
1	1.52	1	0	0.2818	0.153 6	0.115 4	0.8785
1	1.52	1.33	0.659	0.2074	0.098 60	0.069 93	0.7913
1	1.52	1.47	0.733	0.2043	0.094 94	0.066 13	0.7853

the same azimuthal angle as the detector is proportional to $1/\sin\theta$; thus the $\sin\theta$ factors cancel and the detected intensity is proportional to $P(\mu)$. If the sample is uniformly illuminated, as assumed for Eqs. (2.6)–(2.8), the measured signal is also proportional to the area from which detected photons emerge. This can lead to additional angular dependence, for example, if imaging optics are employed that must be either accounted for or eliminated. Our solution of this problem is to illuminate the sample with a narrow beam and to arrange the collection optics so that the detection probability is independent of *where* on the sample face the diffusely transmitted photons happen to originate.

Rather than rotate the collection optics and detector, we find it more convenient to rotate the sample and illumination optics. Sample cells are thus placed vertically at the center of a rotation stage and the angular position is computer controlled by an indexer and stepper motor combination. The output end of a fiber optic bundle is also mounted on the stage, normal to the sample, along with a collimating lens and a photodiode for monitoring drifts in either the source intensity or fiber throughput. For collecting the transmitted light, a large-diameter lens is fixed to the optical table and a photomultiplier tube is placed at its focal point. Thus all light parallel to the optical axis, and therefore exiting at the same angle with respect to the sample normal, is focused onto the detector independent of where on the sample face it originated.

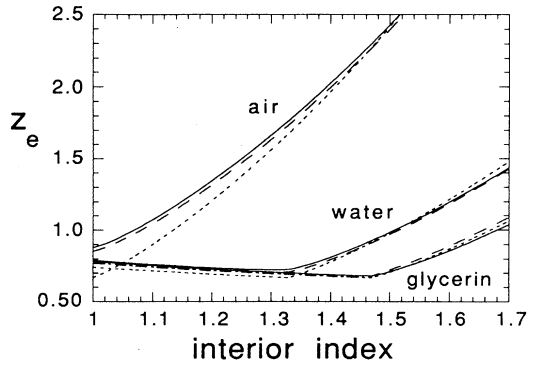

FIG. 1. Extrapolation length ratio vs interior refractive index predicted from Eqs. (2.3), (2.4), and (2.9) for samples held in air, water, or glycerin baths, as labeled. Solid curves are for glass walls of index 1.52, dashed curves are for quartz walls of index 1.46, and dotted curves are for walls of zero thickness.

The angular resolution is controlled by an iris in front of the detector. For the experiments presented here, the output of a HeNe laser at $\lambda=632.8$ nm or an Ar^+ laser at $\lambda=488.0$ nm is chopped and sent into the fiber bundle. Line filters and lock-in detection are employed to reduce background and increase the signal to noise ratio.

The general experimental procedure is to record the measured signal at finely spaced angles throughout the range $-\pi/2<\theta<\pi/2$. Data are checked for symmetry about the normal direction, averaged at equivalent $\pm\theta$ positions, and then normalized by numerical integration to give the probability distribution $P(\mu)$ vs $\mu=\cos\theta$.

IV. EXPERIMENTAL RESULTS

We measure three distinct samples, glass frits, colloidal suspensions, and foams, each having different scattering properties and boundary effects. In all cases the sample geometry is a slab with thickness greater than $7l^*$ and lateral dimensions sufficiently large that incident photons are either backscattered or transmitted; essentially no photons escape out the sides or are absorbed.

A. Glass frits

The first of the three samples we investigate are the easiest to handle and turn out to have the simplest angular distribution for transmitted light. Glass frits are a disordered porous solid made of sintered glass beads or fibers. The large, randomly oriented, glass-air interfaces are responsible for scattering incident photons and account for their opaque, white appearance. Our frits consist of 59% borosilicate glass, BK7, by volume and have pore diameters within the narrow range 40–60 μm. Figure 2 shows angular distribution data at $\lambda=632.8$ nm for one such frit, having a disk geometry of thickness 4.9 mm and diameter 40 mm (GM Associates Inc., Oakland, CA). The data are plotted as $P(\mu)/\mu$ vs μ, revealing a linear relationship independent of polarization. Identical results are found for other samples of the same frit material, independent of thickness or illuminating wavelength, and similar results are found for quartz frits or frits of different porosity. The angular distribution is thus very well described by the simple diffusion theory prediction [Eq. (2.8)] for the case of angle- and polarization-independent boundary reflectivity and no refraction. A fit to this form is displayed as a dashed line through the data in Fig. 2, giving $z_e=1.85$. The corresponding con-

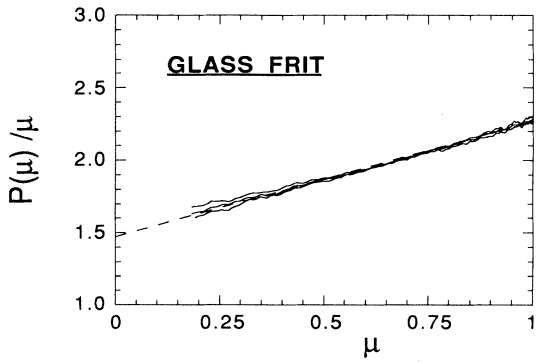

FIG. 2. Angular distribution of total, S-, and P-polarized light diffusely transmitted through a glass frit and an angle $\cos^{-1}\mu$ from the normal. Solid curves represent all three, nearly indistinguishable, measurements. The dashed line is a fit according to the diffusion theory prediction Eq. (2.8), assuming angle- and polarization-independent boundary reflectivity and no refraction.

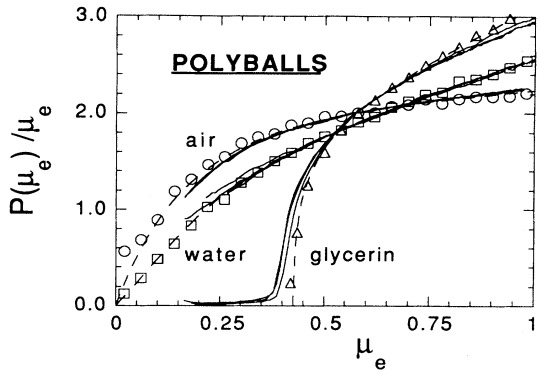

FIG. 3. Angular distribution of light diffusely transmitted through aqueous suspensions of polystyrene spheres placed in glass cells and held in various baths as labeled, using unpolarized detection. Indistinguishable solid curves represent data for 91- and 482-nm-diam spheres, 1- and 2-mm slab thicknesses, and illumination at $\lambda=488.0$ and 632.8 nm. Dashed curves represent the diffusion theory prediction of Eq. (2.6) and symbols represent results of random walk computer simulations, for the known refractive index profiles. Theory, experiment, and simulation all agree with no adjustable parameters.

stant boundary reflectivity is $R=0.47$, which is a reasonable number but cannot be justified in detail since the structure of the frit boundary and the nature of the light propagation within the pore and glass portions are all unknown. Surface roughness must be on the order of the pore size, which is much greater than λ, and must effectively scramble all polarization and angle dependence of the boundary reflectivity and eliminate refraction effects. Thus Eq. (2.8), which has been shown by random-walk computer simulations to accurately describe the angular distribution of diffusely transmitted photons for such an ideal case, applies directly to a class of real physical systems as well.

B. Colloidal suspensions

To more severely confront the diffusion theory prediction with experiment, we next investigate aqueous suspension of polystyrene spheres (polyballs) with known scattering properties and well-defined boundary structures. Since the refractive index of polystyrene [18] is considerably greater than that of water [19], incident light will be strongly scattered according to the sphere diameter and wavelength of light [20]. We use spheres of diameter 91 nm, which are much smaller than λ and therefore scatter light almost isotropically $l^* \cong l_s$, as well as spheres of diameter 482 nm, which scatter light preferentially into the forward direction $l^* \gg l_s$ (Duke Scientific Corp., Palo Alto, CA). Polystyrene to water volume fractions are chosen so that l^* is small compared to the interior thickness of the glass sample cells $L=1$ or 2 mm. Light scattering parameters calculated using Mie theory are summarized in Table II for these samples at the two wavelengths used. To vary the exterior refractive index, and thus alter the boundary conditions of the diffuse light while keeping the suspension and inner boundary constant, cells are mounted in air or are immersed in baths of water or glycerin held in a cylindrical glass tank on the center of the rotation stage. Boundary reflectivity moments and extrapolation length ratios calculated from Eqs. (2.3), (2.4), and (2.9) are collected in Table I for these cases.

TABLE II. Light scattering parameters predicted by Mie theory for the measured aqueous suspensions of polystyrene spheres.

D (nm)	ϕ (%)	λ (nm)	l^* (μm)	l^*/l_s
91	3.5	488.0	136	1.12
91	3.5	632.8	380	1.07
482	1.45	488.0	171	7.25
482	1.45	632.8	127	5.28

The measured angular distributions for light diffusely transmitted through the polystyrene suspensions are shown in Fig. 3 for unpolarized detection. Evidently, the results are significantly different for the three distinct exterior conditions, showing the importance of properly treating reflections from the outer glass interface, but are completely independent of both the optical thickness L/l^* and the scattering anisotropy l^*/l_s. The former served primarily as a check on experimental procedure, while the latter is a crucial test since the diffusion theory prediction relies on the assumption of isotropic scattering. It also serves to refute claims [6,7] that scattering anisotropy is responsible for the form of $P(\mu_e)$. Note also that none of the measured distributions can be described by the simple form obtained for the glass frits. This is due to the angle dependence of the Fresnel boundary reflectivity for both the inner and outer glass interfaces. In fact, a critical angle beyond which no light is transmitted is even apparent for samples immersed in glycerin. For this case, the sample interior has a lower refractive index $n_i=1.33$ than that of the exterior $n_e=1.47$. Photons that strike the interior boundary at a

perfectly glancing angle must therefore, according to Snell's law, emerge such that the cosine of their exit angle is $\mu_e^{\min}=\sqrt{1-(n_i/n_e)^2}\cong 0.426$, while all other photons must emerge close to the normal, with $\mu_e > \mu_e^{\min}$; this is in reasonable accord with the data in Fig. 3 and thus demonstrates that refraction effects must be incorporated. Values of $\mu_e^{\min}$ for other relevant combinations of interior and exterior conditions are collected in Table I.

The full functional form of the angular distribution of the transmitted light is predicted by Eq. (2.7) in terms of the extrapolation length ratio and the angle-dependent boundary reflectivity according to Eqs. (2.2), (2.3), and (2.9). Note that there are no adjustable parameters since the refractive index profiles are known. As shown by the dashed curves in Fig. 3, these predictions all agree remarkably well with the data. Figure 3 also includes results of random-walk computer simulations carried out as in Ref. [5]. These simulations make no transport approximations and are found to agree almost perfectly with the diffusion theory predictions. Therefore, the barely noticeable deviation between theory and experiment in Fig. 3 cannot be attributed solely to inaccurate diffusion approximations; in fact, near perfect agreement can be attained by slightly adjusting the interior and wall refractive indices.

In Fig. 4 we display the angular distribution of S- and P-polarized light transmitted through the same polystyrene suspensions. By contrast with the frits in Sec. IV A, there is noticeable polarization dependence, especially when sample cells are held in air. In all cases, the angular distribution data agrees well with the diffusion theory prediction of Eq. (2.6) with no adjustable parameters. This implies that there is essentially no polarization dependence in the actual photon concentration field, as assumed in the diffusion approximation and in the random-walk simulations. All polarization dependence in the transmitted light thus arises from the boundary reflectivity. The remarkable success of diffusion theory in quantitatively predicting the complicated functional form of the diffusely transmitted light in all these cases validates the extrapolation length ratios collected in the first half of Table I and their use in Eqs. (1.2)–(1.3) for analysis of DTS and DWS data on aqueous colloidal suspensions.

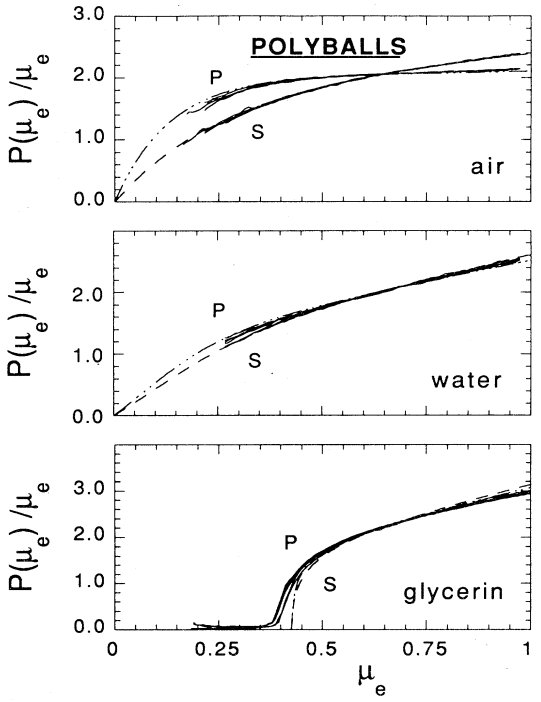

FIG. 4. Angular distribution of S- and P-polarized light diffusely transmitted through aqueous suspensions of polystyrene spheres placed in glass cells and held in various baths as labeled. Data are shown by solid curves, as in Fig. 3, while the diffusion theory predictions of Eq. (2.6) for the known refractive index profiles are shown by dashed curves for S-polarized light and dot-dashed curves for P-polarized light.

C. Aqueous foams

The last type of material we examine is an aqueous foam consisting of fine gas bubbles randomly dispersed in a surfactant solution [21]. We use a commercial shaving foam, Gillette Foamy Regular (The Gillette Co., Boston, MA), which is highly reproducible and whose structure, dynamics, and evolution have been previously studied by DTS and DWS [22–26]. For this material, the gas bubbles occupy a volume fraction of about 92% and have an initial average diameter of 30 μm. With time, the average grows by the diffusion of gas from smaller to larger bubbles; drainage and film rupture are negligible. For measurement of the angular distribution of diffusely transmitted light, foam samples are sealed in glass sample cells of thickness $L=4$ or 7 mm, which is much greater than the transport mean free path of the incident light as given by approximately 3.5 times the average bubble diameter [22].

The primary goal of the measurements presented in this section is not to provide a further test of the diffusion theory predictions, already shown above to be remarkably accurate, but rather to characterize the boundary of the foam so that diffusing light spectroscopies can be more accurately applied. The general procedure demonstrated here can be applied to other unknown systems as well. Since foam is almost entirely gas, a reasonable first hypothesis is that the boundary consists of a stratified dielectric profile, as for the colloidal suspensions, but now with interior index of 1, wall index of 1.52, and exterior index of either 1, 1.33, or 1.47, depending on the bath in which it is immersed. Reflectivity moments and extrapolation length ratios for these cases are collected in the second half of Table I.

The measured angular distributions of light diffusely transmitted through foam contained in glass sample cells are shown in Fig. 5 for unpolarized detection. When held in air, the functional form of $P(\mu_e)/\mu_e$ vs μ_e is gently curved, similar to that for the colloidal suspensions held in air. When immersed in water, by contrast, the functional form falls quickly away from the maximum at $\mu_e=1$ and then displays a pronounced kink near $\mu_e\cong\frac{2}{3}$,

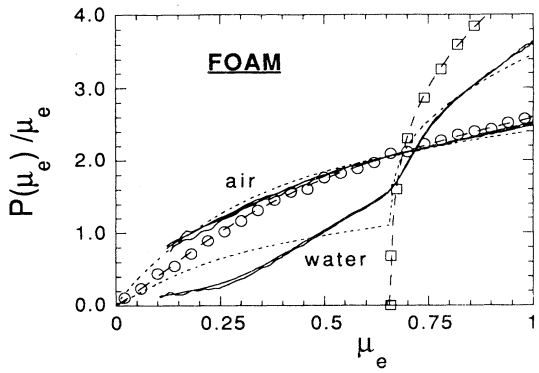

FIG. 5. Angular distribution of light diffusely transmitted through aqueous foam samples placed in glass cells and held in air and water, as labeled, using unpolarized detection. Indistinguishable solid curves represent data for foam at ages ranging from 300 to 1500 min, slab thicknesses of $L=4$ and 7 mm, and illumination at $\lambda=488.0$ and 632.8 nm. Dashed curves represent the diffusion theory predictions of Eq. (2.6) and symbols represent results of random walk computer simulations, for the known exterior and wall refractive indices and assuming an interior refractive index of 1. Dotted curves represent the diffusion theory predictions of Eq. (4.2) for $f_a=0.47$.

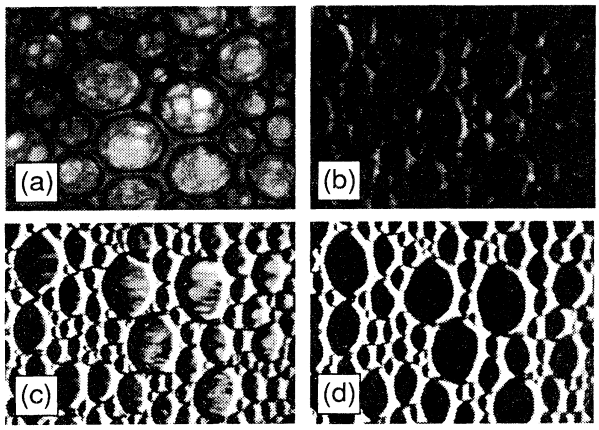

FIG. 6. Photographs of an aqueous foam sample contained in a glass sample cell and immersed in water; images were taken using diffusely transmitted light at (a) 0°, (b) 40°, (c) 48°, and (d) 60° from the sample normal. The largest bubbles shown are approximately 2 mm in diameter. Near the forward direction, most of the light emerges from inside the gas bubbles, while away from the normal, most light emerges from the aqueous solution residing between bubbles.

followed by a slower decay. These results are independent of incident wavelength, cell thickness, and foam age. This behavior can be compared with predictions from diffusion theory and random-walk simulations based on stratified dielectric profiles, as shown also in Fig. 5 by dashed curves. For both exterior conditions shown, the predictions systematically differ with the data, very dramatically for the case of immersion in water. This failure cannot be attributed to the diffusion approximations, however, since the predictions and the random-walk simulation results are indistinguishable. Also, it cannot be attributed to the approximation of an effective interior refractive index of $n_i=1$, since agreement cannot be attained by adjusting the value of n_i. Therefore, the assumption that the boundary consists of a spatially homogeneous stratified dielectric profile must be unwarranted.

The nature of the boundary is revealed in Fig. 6 by photographs made from light diffusely transmitted at various angle. To obtain good images, a foam with an average bubble diameter of 2 mm, much larger than for Gillette Foamy, was first produced by placing an aqueous solution of sodium dodecylsulfate in a rectangular glass cell and vigorously shaking. The cell was then immersed in an aquarium filled with water and illuminated with white light from behind. Photographs were taken vs exit angle from a distance of 40 cm using a 35-mm camera with telephoto lens at the smallest aperture setting; this ensured that the collected light was approximately collinear. In the normal directional, as seen in Fig. 6(a), most of the transmitted light emerges from the interior of gas bubbles pressed up against the glass wall of the sample cell. At angles progressively further from the normal [Figs. 6(b)–6(d)] less and less of the transmitted light originates from within the gas bubbles. Finally, far from the normal as in Fig. 6(d), essentially all of the light emerges from the aqueous solution residing in the soap films and plateau borders between bubbles. This behavior is due to Snell's law, since light that strikes the boundary from inside a bubble can only emerge with $\mu_e > \mu_e^{\min} \cong 0.659$, as set by the refractive indices of the gas bubbles and the water bath; note that the value of $\mu_e^{\min}$ is very close to the location of the kink in the $P(\mu_e)/\mu_e$ data of Fig. 5. Identical behavior can be seen by close inspection of the shaving foam, but is not as readily photographed due to the smaller bubble sizes.

This phenomenon can be modeled within diffusion theory by constructing an appropriate average over *two* stratified dielectric profiles having common wall and exterior refractive indices n_w and n_e, respectively. We thus introduce a single adjustable parameter f_a for the probability for diffuse photons to strike the boundary from inside a gas bubble with index $n_a=1$ and we define a complementary parameter $f_b \equiv 1-f_a$ for the probability for diffuse photons to strike the boundary from inside the aqueous solution with index $n_b=1.33$. Since the glass wall of our sample cell is much thicker that the average bubble size, f_a also represents the probability for a photon traveling toward the foam from within the wall to encounter a gas bubble rather than a soap film or plateau border. All such possible reflections must be considered for self-consistent computation of the extrapolation length ratio from reflectivity moments via Eqs. (2.3) and (2.4). Were it not for such mixing, the reflectivity moments of the two separate stratified profiles given in Table I could be averaged according to f_a. Instead, we must

separately consider the reflection probabilities $R_a(\mu_i)$ and $R_b(\mu_i)$ for photons striking the interior boundary at angle $\cos^{-1}\mu_i$ from inside the two materials with indices n_a and n_b, respectively. Incoherent summation over all possible multiple reflections gives

$$R_a(\mu_i)=\frac{R_{aw}+R_{ew}-(1+f_a)R_{aw}R_{ew}-f_bR_{bw}R_{ew}}{1-f_aR_{aw}R_{ew}-f_bR_{bw}R_{ew}} \quad (4.1)$$

and an analogous expression for $R_b(\mu_i)$, where R_{xy} is the Fresnel reflection probability for the xy interface at the appropriate angle and similarly for the other terms. The total boundary reflectivity is thus $R(\mu_i)=f_aR_a(\mu_i)+f_bR_b(\mu_i)$ and computation of z_e from Eqs. (2.3) and (2.4) for the specified refractive indices and value of f_a is then straightforward.

It is also straightforward to repeat the arguments of Sec. II for the angular distribution of the diffusely transmitted light. It is crucial, however, to recognize that in order for photons to emerge at the same exit angle, they must strike the innermost glass boundary at different angles from inside gas bubbles than from inside the aqueous solution. Using superscripts to distinguish interior angles for these two cases, the probability $P_D(\mu_e)d\mu_e$ for a transmitted photon of polarization state D to exit between $\cos^{-1}\mu_e$ and $\cos^{-1}(\mu_e+d\mu_e)$ from the exterior normal is given by

$$P_D(\mu_e)/\mu_e \propto f_a\left[\frac{n_e}{n_a}\right]^2(z_e+\mu_i^a)[1-R_a^D(\mu_i^a)] + f_b\left[\frac{n_e}{n_b}\right]^2(z_e+\mu_i^b)[1-R_b^D(\mu_i^b)]\,, \quad (4.2)$$

where z_e depends on the value of f_a as described above. The proportionality constant is set by normalization. While this treatment assumes that there is a well-defined extrapolation length ratio for the photon concentration field, it does not assume that the concentration of photons is the same inside as outside the gas bubbles. If this happens to be the case, then f_a is simply the area fraction of the boundary covered by the material with refractive index n_a.

The self-consistent diffusion theory predictions of Eq. (4.2) can be fit to measurements of the angular distribution of diffusely transmitted light for foam samples contained in glass cells and held in either air, water, or glycerin. The resulting values of f_a and z_e for all three exterior conditions are collected in Table III along with the rms deviations based on different sample thicknesses, ages, and illuminating wavelengths. Except for P-polarized light transmitted through samples held in air, we find a single consistent result of $f_a=0.47\pm0.02$; the corresponding extrapolation length ratios are $z_e=1.24\pm0.03$ for air, $z_e=0.751\pm0.002$ for water, and $z_e=0.739\pm0.002$ for glycerin. The angular distribution predicted by Eq. (4.2) at these values is compared with the actual data in Fig. 5 for unpolarized detection. While not perfect, the level of agreement is far better than in the previous treatment, where we effectively assumed $f_a=1$. In particular, note that for the case of immersion in water our treatment reasonably reproduces the observed kink in the data at $\mu_e^{\min}\cong0.66$, below which light cannot emerge from the interior of the gas bubbles due to Snell's law. The systematic deviation still present could be accounted for by two effects not included in our treatment. First, the gas bubbles are rounded, rather being pressed flat up

TABLE III. Results for f_a from fitting Eq. (4.2) to data for the angular distribution of light transmitted through foam samples for the specified exterior index n_e and polarization state D. Apart from the anomalous result for $n_e=1$ and P-polarized detection, we find a single consistent value of $f_a=0.47\pm0.02$; the corresponding extrapolation length ratios are $z_e=1.24\pm0.03$ for air, $z_e=0.751\pm0.002$ for water, and $z_e=0.739\pm0.002$ for glycerin.

n_e	D	f_a	z_e
1	unpolarized	0.71±0.05	1.05
1	S	0.48±0.03	1.23
1	P	0.95±0.05	0.91
1.33	unpolarized	0.47±0.03	0.751
1.33	S	0.45±0.02	0.749
1.33	P	0.49±0.02	0.752
1.47	unpolarized	0.46±0.04	0.738
1.47	S	0.44±0.05	0.737
1.47	P	0.49±0.06	0.741

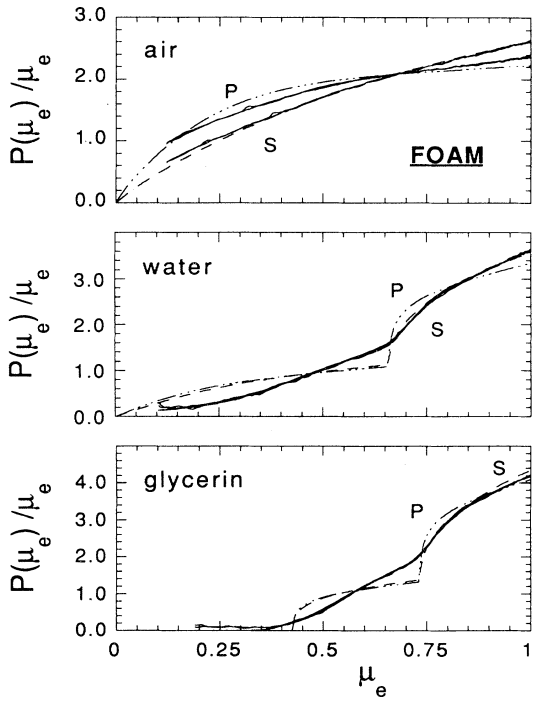

FIG. 7. Angular distribution of S- and P-polarized light diffusely transmitted through aqueous foam samples placed in glass cells and held in various baths as labeled. Data are shown by solid curves, as in Fig. 5, while the diffusion theory predictions of Eq. (4.2) with $f_a=0.47$ are shown by dashed curves for S-polarized light and by dot-dashed curves for P-polarized light.

against the glass walls, as evident in the photographs of Figs. 6(b)–6(d) from the asymmetric shading of individual bubbles. This could cause the rounding of the kink seen near $\mu_e^{\min}$. Second, the aqueous films and plateau borders at the boundary tend to be oriented perpendicular to the glass walls. This could cause the enhancement of emission toward the forward direction in comparison with Eq. (4.2), as observed, especially if photons become trapped in the final films and borders by total internal reflection.

The predictions of Eq. (4.2) at $f_a = 0.47$ are also compared with the measured angular distribution data in Fig. 7, but now for the cases of *S*- and *P*-polarized detection. Again, our treatment reasonably reproduces the major features of the data, except, as in Fig. 5, that more light goes into the forward direction and that the kinks at $\mu_e^{\min}$ are rounded. Note that for the case of immersion in glycerin, not only is there a kink at $\mu_e^{\min} \cong 0.73$ below which no light can escape from inside bubbles due to the gas-glycerin index mismatch, but no light can even escape from inside the aqueous solution below $\mu_e^{\min} \cong 0.43$ due to the water-glycerin index mismatch. Along with the photographs of Fig. 6, this provides direct support for our treatment of the boundary in terms of two refractive index profiles coupled through multiple reflections. A final note is that for all three exterior conditions studied, the level of agreement between Eq. (4.2) and the data is always better for *S*- than for *P*-polarization detection. In particular, the deviation for *P*-polarized light when samples are held in air appears in a similar, though less pronounced, form when the samples are immersed in water or glycerin. This may account for the one anomalous fitting results for f_a listed in Table III and, if so, would give more confidence in use of the single average value $f_a = 0.47 \pm 0.02$ and the resulting extrapolation length ratios for analysis of DTS and DWS data via Eqs. (1.2) and (1.3).

V. CONCLUSIONS

In spite of relying on several uncontrolled approximations, the diffusion theory predictions for the angular distribution of diffusely transmitted light are quantitatively accurate to a surprisingly high degree when compared with experiment. This success validates the treatment of the boundary conditions of the diffuse photon concentration field in terms of an extrapolation length ratio z_e. If the angle and polarization dependence of the boundary reflectivity are known, as for the case of polystyrene suspensions studied in Sec. IV B, then the value of z_e is determined by Eq. (2.4) and the result can be confidently used in Eqs. (1.2) and (1.3), for analysis of DTS and DWS data, and in Eq. (2.6), for the angular distribution of the diffusely transmitted light. If the nature of the boundary is not known in advance, as for the case of the glass frits and foam samples studied in Secs. IV A and IV C, the proper treatment of z_e can be deduced to some extent by measurement of the angular distribution of the diffusely transmitted light. For example, if the transmitted light is completely unpolarized and if $P(\mu_e)/\mu_e$ is linear in μ_e, then it is reasonable to suppose that refraction is not important. The value of z_e can be found by fitting angular distribution data to the simple form in Eq. (2.8). By contrast, if the transmitted light is not unpolarized or if $P(\mu_e)/\mu_e$ is not linear in μ_e, then a significant portion of the boundary may consist of stratified dielectric profile and refraction effects must be considered using Eq. (2.6). Knowledge of the interior refractive index is then crucial and can be gained by immersing an unknown sample in baths having different refractive indices and measuring the angle at which the transmission vanishes. If the boundary is known to be spatially homogeneous, the value of z_e can then be deduced by self-consistently calculating reflectivity moments using experimental data for $P(\mu_e)/\mu_e$ and Eq. (2.6). Images with spatial resolution smaller than the transport mean free path, formed using diffusely transmitted light, can also provide useful clues as to the nature of the boundary, as demonstrated for the foam samples in Sec. IV C. The knowledge of z_e gained by analysis of such measurements is crucial if diffusing light is to be used for quantitatively accurate spectroscopies of the structure and dynamics of opaque materials.

ACKNOWLEDGMENTS

This work was partially supported by NASA and the Petroleum Research Fund.

[1] S. Chandrasekhar, *Radiative Transfer* (Dover, New York, 1960).
[2] P. M. Morse and H. Feshbach, *Methods of Theoretical Physics* (McGraw-Hill, New York, 1953).
[3] M. M. R. Williams, *Mathematical Methods in Particle Transport Theory* (Butterworths, London, 1971).
[4] A. Ishimaru, *Wave Propagation and Scattering in Random Media* (Academic, New York, 1978), Vol. 1.
[5] D. J. Durian, Phys. Rev. E **50**, 857 (1994).
[6] S. McMurry, D. Weaire, J. Lunney, and S. Hutzler, Opt. Eng. **33**, 3849 (1994).
[7] S. McMurry, D. Weaire, J. Lunney, and S. Hutzler, Opt. Eng. **34**, 3345 (1995).
[8] D. J. Durian, Opt. Eng. **34**, 3344 (1995).
[9] P. D. Kaplan, A. D. Dinsmore, A. G. Yodh, and D. J. Pine, Phys. Rev. E **50**, 4827 (1994).
[10] D. A. Weitz and D. J. Pine, in *Dynamic Light Scattering: The Method and some Applications,* edited by W. Brown (Clarendon, Oxford, 1993), p. 652.
[11] D. J. Durian, Appl. Opt. **34**, 7100 (1995).
[12] D. J. Durian, Phys. Rev. E **51**, 3350 (1995).
[13] R. Aronson, SPIE Proc. **1888**, 297 (1993).
[14] T. M. Nieuwenhuizen and J. M. Luck, Phys. Rev. E **48**, 569 (1993).

[15] J. X. Zhu, D. J. Pine, and D. A. Weitz, Phys. Rev. A **44**, 3948 (1991).
[16] R. Aronson, SPIE Proc. **1641**, 72 (1992).
[17] M. Born and E. Wolf, *Principles of Optics* (Pergamon, Oxford, 1980).
[18] *American Institute of Physics Handbook,* edited by D. E. Grey (McGraw-Hill, New York, 1972), p. 6-109.
[19] I. Thormahlen, J. Straub, and U. Grigull, J. Phys. Chem. Ref. Data **14**, 933 (1985).
[20] H. C. van de Hulst, *Light Scattering by Small Particles* (Dover, New York, 1957).
[21] D. J. Durian and D. A. Weitz, in *Kirk-Othmer Encyclopedia of Chemical Technology,* edited by J. I. Kroschwitz (Wiley, New York, 1994), Vol. 11, p. 783.
[22] D. J. Durian, D. A. Weitz, and D. J. Pine, Science **252**, 686 (1991).
[23] D. J. Durian, D. A. Weitz, and D. J. Pine, Phys. Rev. A **44**, R7902 (1991).
[24] J. C. Earnshaw and A. H. Jafaar, Phys. Rev. E **49**, 5408 (1994).
[25] J. C. Earnshaw and M. Wilson, J. Phys.: Condens. Matter **7**, L49 (1995).
[26] A. D. Gopal and D. J. Durian, Phys. Rev. Lett. **75**, 2610 (1995).

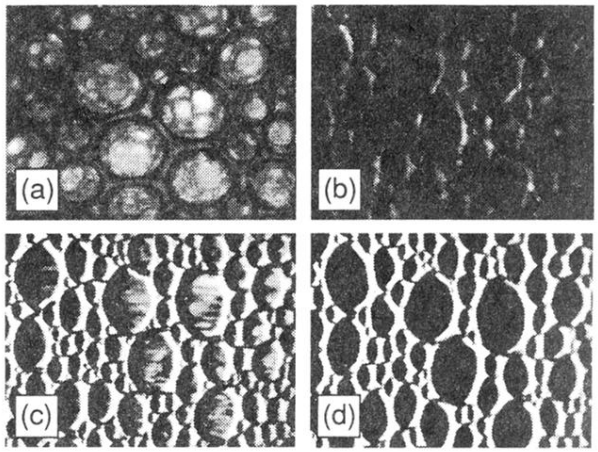

FIG. 6. Photographs of an aqueous foam sample contained in a glass sample cell and immersed in water; images were taken using diffusely transmitted light at (a) 0°, (b) 40° , (c) 48°, and (d) 60° from the sample normal. The largest bubbles shown are approximately 2 mm in diameter. Near the forward direction, most of the light emerges from inside the gas bubbles, while away from the normal, most light emerges from the aqueous solution residing between bubbles.